POD Preprocessing of IR Thermal Data to Assess Heat Source Distributions

N. Ranc · A. Blanche · D. Ryckelynck · A. Chrysochoos

Abstract Infrared thermography is a useful imaging technique for analyzing the thermomechanical behaviour of materials. It allows, under certain conditions, surface temperature monitoring and, via a diffusion model, estimation of heat sources induced by dissipative and/or thermally coupled deformation mechanisms. However, the noisy and discrete character of thermal data, the regularizing effect of heat diffusion and heat exchanges with the surroundings complicate the passage from temperature to heat source. The aim of this paper is to show that the prior use of reduced-basis projection of thermal data improves the signal-to-noise ratio before estimating the heat source distributions. The reduced basis is generated by proper orthogonal decomposition (POD) of physically-admissible thermal fields. These fields are solutions of ideal diffusion problems related to a set of putative heat sources. preprocessing is applied to different direct methods (finite differences, spectral solution, local least-squares fitting) already used in the past. The gain of this preprocessing is determined using a numerical penalizing benchmark test. The methods are finally compared using data extracted from a dynamic cyclic test on a pure copper specimen.

N. Ranc (✉)
Laboratoire PIMM, UMR CNRS 8006, Arts et Métiers ParisTech,
151 Boulevard de l'Hôpital, 75013 Paris, France
e-mail: nicolas.ranc@ensam.eu
URL: http://pimm.paris.ensam.fr/en/user/9

A. Blanche · A. Chrysochoos
LMGC, UMR CNRS 5508, CC 048, Université Montpellier 2,
Place Eugène Bataillon, 34095 Montpellier Cedex 05, France

D. Ryckelynck
Centre des matériaux, UMR CNRS 7633, Mines ParisTech,
10 rue Henry Desbrueres, BP 87, 91003 Evry Cedex, France

Keywords Infrared thermography · Quantitive image processing · Dissipation fields · Thermomechanical couplings · Behavior modeling · Proper orthogonal decompsition

Introduction

Temperature variations induced by the deformation of solid materials come from heat sources of different natures. Sources related to energy dissipation can be distinguished from those induced by strong thermo-mechanical couplings. Dissipation reflects the irreversibility of the deformation process while coupling sources indicate the strong interdependence of thermal, mechanical and microstructural states. It should be noted that temperature variations depend on the intensity and distribution of heat sources within the material but also on the heat diffusion parameter and the heat exchange conditions with the surroundings. These temperature variations are thus not completely intrinsic to the material behavior. It is therefore of interest to develop image processing methods able to assess heat sources using surface temperature measurements generated by an infrared camera. To obtain quantitatively reliable thermal fields is not easy and the advent of infrared focal plane array (IRFPA) cameras, which are certainly faster and more sensitive than cameras equipped with a single liquid nitrogen cooled detector and a scanning system, has not simplified the situation from a metrological standpoint. The main reason is that the response of matrix elements to a uniform thermal scene is currently not uniform. We will not discuss these complicated of IR metrology issues here and interested readers are referred to recent works on this topic [2, 9, 26]. However, it should be noted that an IR camera is not directly a measuring device and any quantitative use of

thermal data requires some precautions. Depending on the intended application and the studied material, it is crucial to:

- Check the thermal stability of the thermographic system;
- Calibrate the complete measurement chain, with the camera and optics being thermally stable. A pixel calibration is highly recommended;
- Know the emissivity of the studied material surface;
- Determine the spatial resolution of the camera in the optical conditions of use;
- Check the frame rate and number of recorded images.

The link between the temperature and the heat source fields is provided by the heat diffusion equation:

$$\rho C_\alpha \dot{T} - \text{div}\left(k\,\overrightarrow{\text{grad}}\,T\right) = d_1 + s_{thm} + r_e, \tag{1}$$

where ρ denotes the mass density, C_α the specific heat at constant mechanical and micro-structural state variables, T the absolute temperature, k the heat conduction tensor, d_1 the intrinsic dissipation, s_{thm} the thermo-mechanical coupling sources, and r_e the possible volume external heat rate supply. The left hand member of equation (1) consists of partial derivatives of the temperature weighted by thermophysical parameters characterizing the material. The quality of the heat source assessments thus depends on the accuracy of the temperature measurements but also on the knowledge of the thermophysical parameters. Substantial effort is currently focused on developing thermal methods to estimate these thermophysical parameter fields using inverse methods [16, 17].

So far, the following strong hypotheses have been put forward with respect to computing heat sources during infrared image processing:

- Mass density and specific heat are material constants, independent of the thermodynamic state.
- The heat conduction tensor remains constant and isotropic during the test ($k_{ij} = k\delta_{ij}$).
- The external heat rate supply r_e due to heat exchange by radiation is time-independent, so the equilibrium temperature field T_0 verifies $-k\Delta T_0 = r_e$. It is then convenient to consider the temperature variation ϑ defined by $\vartheta = T - T_0$.

These hypotheses are relevant for many situations, but are inadequate when strong anisotropy pre-exists or develops during strain and when strain and/or damage localization occurs. Alternative hypotheses should be proposed to deal with such situations and ensure reliable calorimetric analysis of the mechanical behavior.

When taking these latter hypotheses into account, the heat equation can be rewritten in the following compact form:

$$\rho C_\alpha \dot{\vartheta} - k\Delta\vartheta = s, \tag{2}$$

where s stands for the overall heat source.

Even in its simplest form, the heat equation (equation (2)) cannot be directly used for estimating heat losses and sources. In fact, cameras only provide information on the specimen surface, which is insufficient to estimate 3D distribution sources without any supplementary information. New concessions are required.

For uniaxial tests performed on thin flat samples, a first possibility is to work with a diffusion equation integrated over the specimen cross-section [14]. The specimen gage length is denoted by L. With $\vartheta(x,t)$ now denoting the mean temperature variation at time t over the cross section $S(x)$, and x being the longitudinal coordinate, the 1D heat diffusion equation can be formulated as:

$$\rho C_\alpha \left(\frac{\partial\vartheta}{\partial t} + \frac{\vartheta}{\tau_{th}^{1D}(x)}\right) - k\left(\frac{S'}{S}\frac{\partial\vartheta}{\partial x} + \frac{\partial^2\vartheta}{\partial x^2}\right) = s(x,t), \tag{3}$$

where $s(x,t)$ is the longitudinal distribution of the mean heat source per cross section S, with S' stands for $\frac{\mathrm{d}S}{\mathrm{d}x}$, and $\tau_{th}^{1D}(x)$ being a time constant characterizing heat losses perpendicular to the specimen axis through the cross-section boundary δS [14]. This latter is defined by:

$$\tau_{th}^{1D}(x) = \frac{\rho C_\alpha S(x)}{2h(e+\ell(x))} = \frac{\rho C_\alpha e\,\ell(x)}{2h(e+\ell(x))}, \tag{4}$$

where h is a heat exchange coefficient between the specimen and the surrounding air, e is the constant thickness of the sample and $\ell(x)$ is its variable width. The plate specimen geometry presented in Fig. 1 is classically used [1] for ultrasonic high cycle fatigue tests.

When dividing equation (3) by ρC_α, the heat diffusion coefficient $D = \frac{k}{\rho C_\alpha}$ appears in the equation and the source term $\frac{s}{\rho C_\alpha}$ is expressed in °C.s^{-1}. This allows us to define, for each type of source, an equivalent heating or cooling speed in adiabatic conditions. This facilitates comparison of

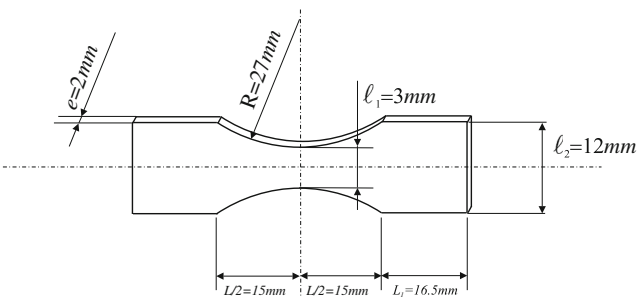

Fig. 1 Specimen geometrical characteristics

different types of source, or of sources of the same type in different materials.

For practical use of equation (3), the mean width-wise temperature variation, measured at the specimen surface, must remain close to the mean temperature over the cross-section S. This assumption is even more relevant when the sources are regularly distributed over S and the Biot number $Bi = \frac{h\ell_c}{k}$ is small compared to the unit. In the Biot number expression, the characteristic length ℓ_c is commonly defined as the volume of the body divided by the surface area and is thus equal to $\frac{e\ell}{2(e+\ell)}$ in the case of an ultrasonic fatigue plate specimen. A Biot number of 10^{-4} can therefore be calculated in our case.

The smoothing (regularizing) effect of heat diffusion is beneficial when it derives sources from thermal measurements performed at the specimen surface. To briefly illustrate this effect qualitatively, we considered a simple 1D steady-state diffusion model, $\tau_{th}^{1D}(x)$ representing the time constant characterizing heat losses in the plane perpendicular to direction Ox (Fig. 2). Although the sources are randomly distributed, the results show that the temperature profile is, comparatively, very regular.

In this euristic example, the chosen thermophysical and geometrical constants were: $\rho = 7800\,kg.m^{-3}$, $C_\alpha = 450\,J.kg^{-1}.K^{-1}$, $k = 60\,W.m^{-1}.K^{-1}$, $L = 0.1\,m$, $\tau_{th}^{1D} = 50\,s$. The overall curvature of the temperature profile is imposed by the Fourier boundary conditions of the form $\frac{\partial\vartheta}{\partial x} \pm \lambda\vartheta = 0$, with $\lambda = 10\,m^{-1}$, reflecting linear heat losses.

It is thus understandable that the reverse temperature to source path is particularly unstable, especially when the thermal data becomes discrete and noisy. To illustrate this, the previous model can be used in the simple case where the temperature profile is reduced to $\vartheta_a(x) = \vartheta_0 \cos(\omega_0 x)$, with ω_0 being the eigenpulsation associated with the first eigenfunction of the partial derivative operator $-\frac{\partial^2}{\partial x^2}$ (see details in the "spectral method" section). Under the boundary conditions, $\omega_0 \tan(\omega_0 L/2)) = \lambda$, $\omega_0 \in]0, \frac{\pi}{2}[$.

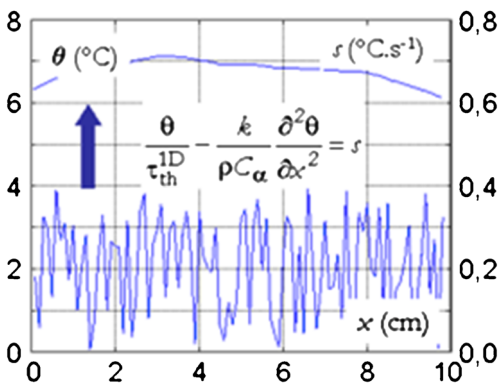

Fig. 2 Regularizing effect of heat diffusion

In Fig. 3(a), analytical, noisy and filtered thermal profiles were shifted (shift = 0.1 °C) in order to facilitate the comparison. We chose white noise, consistent with experimental observations [4], but with a peak-to-peak amplitude of about 0.1 °C, i.e. twofold greater than those often experimentally obtained with current IRFPA cameras in laboratory conditions. Here the signal was fitted using Gaussian convolutive filtering. This method was introduced by Nayroles et al. [24] and the boundary effects were discussed by Chrysochoos and Louche in 2000 [10]. In Fig. 3(b), the profile of the analytically computed sources and that derived using a finite difference (FD) approximation of the diffusion operator using thermal data without noise were plotted. The two curves are almost indistinguishable. The scatter plot represents the estimated sources obtained by finite differences when using the filtered data. The sources computed with the noisy thermal data were not plotted in Fig. 3(b), since the noise on the sources was too great (16 ° C.s^{-1}). Note that even after (low-pass) convolutive filtering, the finite difference method is not very satisfactory. That is why other methods have been proposed. In the past, truncated spectral solutions (SPS) of the heat equation were used [8] as well as local least-squares (LSQ) analytical approximations [5].

In what follows, we show that truncated projection of temperature profiles on an orthonormal numerical base, obtained using a proper orthogonal decomposition (POD) of diffusion problem solutions, helps improve the computation of heat sources regardless of the method used (FD, SPS, LSQ). A set of putative heat sources, that are in practice simulated sources, denoted $\left(s^{(r)}\right)_{r=1,\ldots,M}$, is introduced to define ideal diffusion problems. These sources are possible contributions to experimental heat sources. The solutions to ideal problems are termed physically-admissible thermal fields and are denoted $(\vartheta^{(r)})_{r=1,\ldots,M}$. $\vartheta^{(r)}$ fulfill equation (3) with $s = s^{(r)}$. They span a subspace whose reduced basis is generated using the POD method.

The POD method is based on statistical data analysis [20–22]. Karhunen-Loève Decomposition (KLD) is an other name of the POD method. In [3, 19, 23], the POD method was used in turbulence to extract the salient features of velocity fields. As shown in [12, 25], this method can be applied to the thermal inverse problem without solving any numerical simulation. However, in many previous studies, the POD method has been used to reduce the computational complexity of numerical simulations. Note that POD reduced bases can also handle partial data, as they appear in many experimental measurements. In case of missing data, data reconstructions can be achieved by various methods, e.g. gappy POD [6, 15, 30], POD-EIM [18], DEIM [7] or hyper-reduction [27, 28].

A theoritical analysis of noise reduction provided by POD in thermal measurements can be found in [13]. In

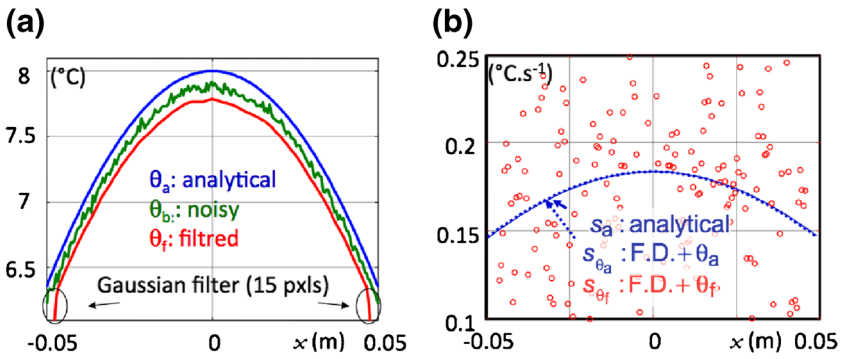

Fig. 3 Heat source assessments (**b**) using thermal data (**a**)

that paper, the POD method is applied to experimental data only. Here, the decomposition we propose to generate the POD basis, does not involve decomposition of experimental data but rather decomposition of solutions related to chosen diffusion problems. These diffusion problems, mathematically defined by equation (3), are assumed to represent the physics we expect to observe. The reduced basis is related to physically admissible thermal fields $\left(\vartheta^{(r)}\right)_{r=1,\dots,M}$, not to experimental data. We do not perform a statistical analysis of the experimental data, contrary to what Del Barrio et al. propose in [13] using the POD.

The reduced basis representation of the temperature field reads:

$$\vartheta(x,t) = \sum_{k=1}^{N} a_k(t)\varphi_k(x), \tag{5}$$

where $(\varphi_k)_{k=1,\dots,N}$ are the proper orthogonal modes (POMs) of the POD reduced basis. They are solutions of the following equation [23]:

$$\varphi_k = \arg\max_{\psi} \frac{\sum_{r=1}^{M} \int_0^{t_f} \left(\int_\Omega \vartheta^{(r)}(x,t)\,\psi(x)\,\mathrm{d}\Omega\right)^2 \mathrm{d}t}{\int_\Omega \psi^2(x)\,\mathrm{d}\Omega}, \tag{6}$$

where Ω is the spatial domain and $[0, t_f]$ is the time interval. This equation means that functions $\psi(x)$ which maximize their projection on throughout the calculated temperature fields $\vartheta^{(r)}$ for every time in $[0, t_f]$ are searched.

There are many solutions to this maximum problem. POMs are ordered such that:

$$\sigma_k^2 = \frac{\sum_{r=1}^{M} \int_0^{t_f} \left(\int_\Omega \vartheta^{(r)}(x,t)\varphi_k(x)\,\mathrm{d}\Omega\right)^2 \mathrm{d}t}{\int_\Omega \varphi_k^2(x)\,\mathrm{d}\Omega}, \tag{7}$$

$$\sigma_k^2 \geq \sigma_{k+1}^2. \tag{8}$$

Here σ_k^2 is the positive eigenvalue related to the POM φ_k. The following orthogonality property is fulfilled:

$$\int_\Omega \varphi_k(x)\,\varphi_p(x)\,\mathrm{d}\Omega = \delta_{kp}, \tag{9}$$

where δ_{kp} is Kroneker's delta symbol. Extensive details on the properties of this approximation can be found in [13].

Energy, according to signal theory, denoted by $\mathcal{E}$ can be introduced as follows:

$$\mathcal{E} = \sum_{r=1}^{M} \int_0^{t_f} \int_\Omega \vartheta^{(r)}(x,t)\,\vartheta^{(r)}(x,t)\,\mathrm{d}\Omega\,\mathrm{d}t. \tag{10}$$

It can be proven that:

$$\mathcal{E} = \sum_{k=1}^{\infty} \sigma_k^2. \tag{11}$$

As N increases, the approximation error decreases, and $\sum_{k=1}^{N} \sigma_k^2$ tends to the energy $\mathcal{E}$.

The construction of the POD basis will be detailed in the first part of this paper. Then, in the second part, a benchmark test with a particular heat source distribution and evolution will be defined, while in the last part the various methods to identify the heat source will be presented and the results compared.

Application of POD Preprocessing to Thermal Data

In the current study, discrete sets of physically admissible thermal fields were analyzed using singular value decomposition (SVD), which is a discrete implementation of POD. As a set of putative heat sources $\left(s^{(r)}\right)_{r=1,\dots,M}$, we consider time-constant point sources in space. These point sources are designed to be observable by IR cameras, while having the smallest spatial support. This support is related to each IR element. Therefore $M = n$, where n denotes the number of IR elements. The discrete values of $\vartheta^{(r)}(x_i, t_p)$ are stored in a matrix denoted Θ. Let us consider the case of a putative heat source $\left(s^{(r)}\right)$, where $\theta^{(r)}$ denotes the matrix of the discrete values of $(\vartheta^{(r)}(x_i, t_p))_{i=1,\dots,n;\ p=1,\dots,m}$, such that:

$$\theta_{pi}^{(r)} = \vartheta^{(r)}\left(x_i, t_p\right),\ i = 1,\dots,n,\ p = 1,\dots,m. \tag{12}$$

Using the SVD, $\theta^{(r)}$ can be decomposed as:

$$\theta^{(r)} = U\Sigma V^T, \tag{13}$$

where U and V are orthonormal matrices ($m \times n$ and $n \times m$, respectively), and Σ is a diagonal matrix. The columns of

the orthogonal matrix V are the computed POMs, denoted by v_k. The diagonal matrix Σ is termed the singular matrix whose elements (along the diagonal) are non-negative numbers, called singular values, arranged in decreasing order (see Fig. 4(a)).

Each of these singular values corresponds to a single basis function v, and represents the level of 'energy' of the associated mode. In Fig. 4(b), the first four modes are plotted. The matrices U and Σ can be multiplied to form matrix Q and equation (5) can be re-written as:

$$\theta^{(r)} = QV^T = \sum_{k=1}^{n} q_k v_k^T, \tag{14}$$

where q_k and v_k are column matrices that are, respectively, the discrete representation of the functions $a_k(t)$ and $\varphi_k(x)$ of the continuous temperature field.

The singular values can be used to derive a lower order model by establishing a reduced order matrix, Σ_{red}, that contains the first N ($N \leq n$) singular values with the rest of the diagonal entries set at zero. The model order N can be set to capture the desired percentage of total 'energy' in the system. In our case, this operation will eliminate much of the thermal white noise that is assumed to mainly be associated with the multiple modes of low 'energy'.

The matrix Θ was considered to construct the reduced basis related to the physically admissible thermal fields. This involves all discrete thermal responses associated with the point sources mentioned above, such that:

$$\Theta^T = \left[\theta^{(1)T}, \theta^{(2)T}, \ldots, \theta^{(n)T}\right] \tag{15}$$

Each elementary thermal dataset $\theta^{(r)}$ is the discrete solution of the following diffusion problem already defined in equation (3):

$$\begin{cases} \rho C\left(\dfrac{\partial \vartheta^{(r)}}{\partial t} + \dfrac{\vartheta^{(r)}}{\tau_{th}^{1D}(x)}\right) - k\left(\dfrac{S'}{S}\dfrac{\partial \vartheta^{(r)}}{\partial x} + \dfrac{\partial^2 \vartheta^{(r)}}{\partial x^2}\right) = s_0\delta(x - x_r), \\ \vartheta^{(r)}\left(-\frac{L}{2}, t\right) = \vartheta^{(r)}\left(\frac{L}{2}, t\right) = 0 \\ \vartheta^{(r)}(x, 0) = 0 \end{cases} \tag{16}$$

where s_0 is an arbitrary positive constant, $\delta(x)$ the Dirac distribution, and $x_r = -\frac{L}{2} + r\Delta x$ with $\Delta x = \frac{L}{n+1}$ and $1 \leq r \leq n$ the localization of the point source.

To compute the POMs v_k, we considered the matrix $\widehat{\Theta} = \Theta\Theta^T$ to reduce the size of the thermal data to be processed. SVD corresponds to the eigenvalue decomposition (EVD) for this type of symmetric matrix.

Note that the basis of v_k is computed once and for all for a given form of diffusion problem. Another advantage is that the prior determination of the order N can be fixed for a given signal-to-noise ratio. Once N is defined, the projection of the thermal data derived from the tests is limited to the first N orthogonal modes.

Benchmark Test

A baseline test was set up to estimate the gain offered by the preprocessing of thermal data by POD and compare the reliability of the different heat source computations. Penalizing conditions were systematically chosen to also check the robustness of the heat source assessment.

Regarding the spatiotemporal distribution of sources, a highly heterogeneous field was defined with respect to space that quite slowly varies with respect to time. The analytical expression of $s_{ref}(x, t)$ reads:

$$s_{ref}(x, t) = s_0\left(\frac{1}{2} - \frac{x}{L}\right)e^{-\frac{6|x|}{L}}\left(1 - e^{-\frac{t}{t_0}}\right)\left|\sin\left(2\pi\left(\frac{2x}{L} + \frac{t}{t_1}\right)\right)\right|, \tag{17}$$

where L is the sample gage length with $-\frac{L}{2} \leqslant x \leqslant \frac{L}{2}$. Constants appearing in the reference source are $s_0 = 29\,°\text{C}.s^{-1}$, $t_0 = 5\,s$, $t_1 = 5 \times 10^3\,s$. Sources are always positive and two moving source peaks can be seen in Fig. 5(a) and (c). Progressive saturation of the heat source intensity was also planned.

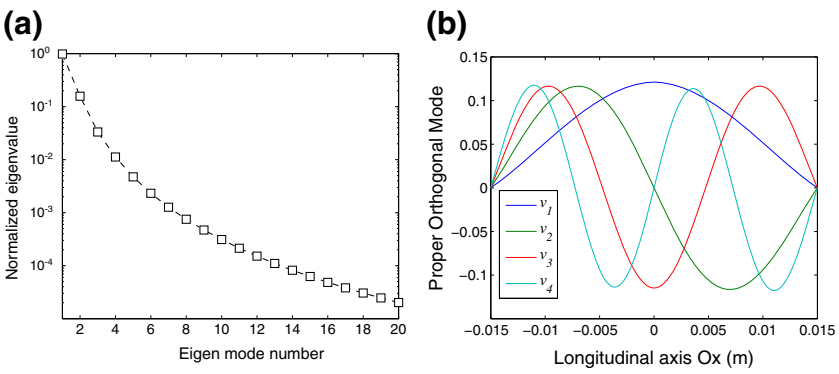

Fig. 4 Results of SVD decomposition (**a**) Example of a normalized distribution of singular values $\frac{\Sigma_k}{\sqrt{\mathcal{E}}}$ (**b**) Example of the first proper orthogonal modes

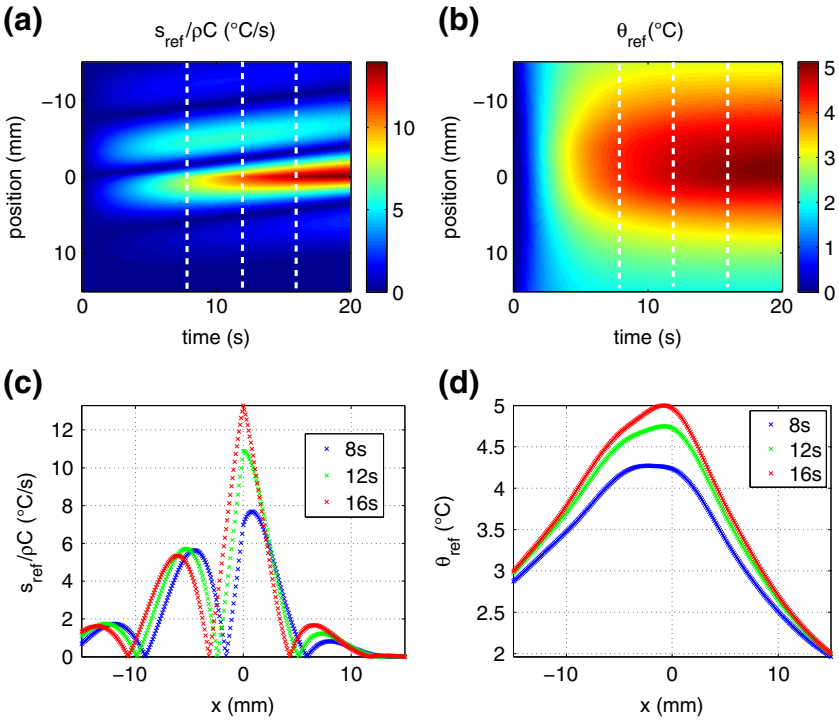

Fig. 5 Benchmark test: (**a**) space-time distribution of heat sources, (**b**) corresponding temperature distribution (**c**) heat sources and (**d**) temperature profiles at times $t_j = 8, 12, 16s$; these captures are shown by *dashed lines* in the color mapping (**a-b**)

Non-homogeneous dissymmetric Dirichlet boundary conditions were also chosen in order to take possible warming of the specimen by the grips of the testing machine into account:

$$\vartheta_{ref}(-L/2,t) = \vartheta_0^- \left(1 - \mathrm{e}^{-\frac{t}{t_0^-}}\right) \quad \text{and}$$
$$\vartheta_{ref}(+L/2,t) = \vartheta_0^+ \left(1 - \mathrm{e}^{-\frac{t}{t_0^+}}\right), \tag{18}$$

with $\vartheta_0^- = 3°\mathrm{C}$, $t_0^- = 2.5\,s$, $\vartheta_0^+ = 2°\mathrm{C}$, $t_0^+ = 2\,s$.

Now regarding the material characteristics, we chose the thermophysical constants of pure copper ($\rho = 8920\,kg.m^{-3}$, $C = 385\,J.kg^{-1}.K^{-1}$, $k = 360\,W.m^{-1}.K^{-1}$). Pure copper has a high diffusivity coefficient ($D = \frac{k}{\rho C} \approx 10^{-4}\,m^2.s^{-1}$, i.e. dozens of times greater than that of many conventional materials). The diffusion strongly regularizes the temperature fields, even for very heterogeneous source distributions, thus complicating the inverse heat source assessment. Figure 5(b) and (d) show the evolution of the temperature profile ϑ_{ref} associated with s_{ref}. The lack of heat source around $x = 0$ is, for instance, hard to imagine by looking solely at the thermal response.

A last penalizing parameter considered here was the signal-to-noise ratio (SNR). At first approximation, this is white noise with a uniform distribution. The sensitivity of IR cameras is characterized by the noise-equivalent temperature difference (NETD) measured in milliKelvins (mK). R&D cameras generally have an NETD of about $20\,mK$ at a temperature of 25°C for an aperture time of one millisecond. A noise with a three standard deviations of $50\,mK$ was chosen to further check the robustness of the heat source computations. Note that in the case of 1D heat source analysis, thermal data have to be widthwise averaged (reflecting the mean temperature over the cross-section) to construct the thermo-profile time course. In the case of Gaussian white noise, the noise range decreases with the square root of the number of data considered in the averaging operation. For space resolutions of the IR camera images such that at least 9 pixels are considered to construct the profiles, $50\,mK$ should correspond to a noise with a three standard deviations of about $150\,mK$.

Heat Source Computation

In the introduction, we stressed that the 3D heat diffusion equation (equation (1)) makes a direct link between thermal and calorimetric aspects of deformation mechanisms. From a mathematical standpoint, the determination of heat sources when the surface (i.e. boundary) temperature distribution is a so-called inverse problem that is very difficult, often impossible, to solve because of the regularizing (smoothing) effects of the heat diffusion and the lack of prior information on the heat source distribution. Our first goal was thus to get a simplified heat equation adapted to thin flat specimens, so as to be able to compute

1D distributions of heat sources using surface thermal field measurements (equation (3)). We therefore considered an averaged diffusion equation over the sample cross-section "to convert" surface temperatures into mean heat sources. It is thus a 'direct' computation of heat sources that will be considered hereafter.

Note that different heat source calculation methods have been developed over time. It was not until the end of the 1970s that infrared techniques were used to obtain quantitative results in civil applications. Regarding experimental investigations on the mechanics of materials using digitized infrared data, we ought to mention what is, to our knowledge, the first designed and used homemade analog-digital converter of video signals from IR cameras [24].

At this time, because of the slowness of the first digitization systems of mono-detector cameras used in the 1990s (typically two digitized images per second), spectral solutions (SPS) of the heat equation were used to estimate heat sources [8]. The main advantages of the spectral method is the knowledge of the eigen-functions of the Laplacian operator – typically sine and cosine functions for parallelepipedic specimens – which allows assessment of the conduction heat losses without markedly amplifying the noise (use of truncated solutions to limit noise effects). Fourier's techniques have also been used [10], but they are essentially limited to spatial filtering in the image processing. Convolutive filtering using the discrete Fourier transform were especially used.

The main drawbacks of these techniques were:

- A previous periodic expansion of thermal images, preferable before any heat source computation. This expansion naturally requires a lot of memory space and is time consuming. It is however necessary to avoid supplementary frequencies resulting from the automatic periodization induced by the discrete Fourier transform.
- The impossibility of reducing all noise effects, with thermal noise being centered white noise with a uniform power spectrum. We used a low-pass Gaussian filter, which is a smooth filter even when twice derived (Laplacian computation).

Fitting techniques were more recently developed with IRFPA cameras. Local least-squares approximation of temperature fields using different sets of approximation functions was used: a set of space-time polynomials for monotonous loading [11], trigonometric in time and polynomial functions in space for monochromatic fatigue tests [4]. The optimized sizes of the space-time approximation domain naturally have to be adjusted according to the heterogeneity of the sought heat source distribution and of the signal-to-noise ratio. In what follows, three of these different methods are reused and their results compared after preprocessing of thermal data using POD. Heat source assessments obtained with a simplistic finite difference method were compared to those obtained using a quasi-analytically spectral solution (global approximation) and those stemming from local least-squares approximation (local approximation) of the thermal data.

The three methods start from the same diffusion equation:

$$\frac{s(x,t)}{\rho C} = \frac{\partial \vartheta}{\partial t} + \frac{\vartheta}{\tau_{th}^{1D}(x)} - D\frac{S'(x)}{S(x)}\frac{\partial \vartheta}{\partial x} - D\frac{\partial^2 \vartheta}{\partial x^2}. \tag{19}$$

Finite Differences

The principle of this first method is to estimate the right-hand side of equation (19) directly using thermal data. Finite difference approximations of the different partial derivative operators can be done. When respectively letting Δt and Δx denote the time and space discretization steps, respectively, θ_i^j the temperature variation $\vartheta(x_i, t_j)$, the volume heat source s_i^j can be rewritten as:

$$\frac{s_i^j}{\rho C} = \frac{\theta_i^j - \theta_i^{j-1}}{\Delta t} + \frac{\theta_i^j + \theta_i^{j-1}}{2\tau_{th}^{1D}(x_i)} - D\frac{S'(x_i)}{S(x_i)}\frac{\theta_{i+1}^j - \theta_{i-1}^j}{2\Delta x} - D\frac{\theta_{i+1}^j - 2\theta_i^j + \theta_{i-1}^j}{\Delta x^2}. \tag{20}$$

Note that a forward Euler scheme with respect to time was used in equation (20). We also could have used a backward scheme or any other scheme (e.g. θ method). The first order derivative with respect to space is computed using a second order finite difference scheme consistent with the second order derivative that must also be approximated. This method is particularly easy to program and gives rapid heat sources estimates. It is, however, very sensitive to thermal noise, with the Laplacian term being a powerful noise amplifier.

Spectral Solution

The second method uses the spectral solution ϑ_{sp} of the diffusion problem associated with the following partial derivative problem:

$$\begin{cases} \left(\frac{\partial \vartheta}{\partial t} + \frac{\vartheta}{\tau_{th}^{1D}(x)}\right) - D\left(\frac{S'(x)}{S(x)}\frac{\partial \vartheta}{\partial x} + \frac{\partial^2 \vartheta}{\partial x^2}\right) = \frac{s(t,x)}{\rho C} \\ \vartheta(-\frac{L}{2}, t) = \vartheta^-(t) \quad \text{and} \quad \vartheta(+\frac{L}{2}, t) = \vartheta^+(t) \\ \vartheta(x, 0) = 0 \end{cases} \tag{21}$$

The two boundary conditions ϑ^- and ϑ^+ represent an interpolation of experimental measurements of the temperature in $-\frac{L}{2}$ and in $\frac{L}{2}$. The heat diffusion problem is indeed linear with respect to the temperature. Consequently, it is possible to use a superposition principle. We consider that

the experimental temperature profile $\vartheta(x,t)$ is the result of two contributions $\vartheta_{sp}(x,t)$ and $\vartheta_{lf}(x,t)$.

On the one hand, the temperature variation ϑ_{sp} is the spectral solution of the diffusion problem that takes the heat source distribution into account:

$$\begin{cases} \dfrac{\partial \vartheta_{sp}}{\partial t} - D\dfrac{\partial^2 \vartheta_{sp}}{\partial x^2} = \dfrac{s(x,t)}{\rho C} \\ \vartheta_{sp}\left(-\frac{L}{2},t\right) = \vartheta_{sp}\left(+\frac{L}{2},t\right) = 0 \\ \vartheta_{sp}(x,0) = 0 \end{cases} \tag{22}$$

Here, the heat sources $s(x,t)$ are naturally unknown. To compute the solution ϑ_{sp} homogenous Dirichlet boundary conditions were chosen. In this situation, the sets of eigenfunctions of the Laplacian operator are $(\cos((2k+1)\pi x/L)$ and $\sin(2k\pi x/L), k \in \mathbb{N})$ and ϑ_{sp} can be resolved as follows:

$$\vartheta_{sp}(x,t) = \sum_{k=0}^{\infty}\left(a_k(t)\cos\left(\frac{(2k+1)\pi}{L}x\right) + b_k(t)\sin\left(\frac{2k\pi}{L}x\right)\right), \tag{23}$$

where a_k and b_k are constants which depend only on time.

On the other hand, the construction of ϑ_{lf} is sometimes called the "lifting" of ϑ and is given by the equations:

$$\begin{cases} \dfrac{\partial \vartheta_{lf}}{\partial t} - D\dfrac{\partial^2 \vartheta_{lf}}{\partial x^2} = -\dfrac{\vartheta}{\tau^{1D}} + D\dfrac{S'(x)}{S(x)}\dfrac{\partial \vartheta}{\partial x} = \dfrac{s_{lf}(x,t)}{\rho C} \\ \theta_{lf}(-\frac{L}{2},t) = \vartheta^-(t) \quad \text{and} \quad \vartheta_{lf}(t,+\frac{L}{2}) = \vartheta^+(t) \\ \vartheta_{lf}(x,0) = 0 \end{cases} \tag{24}$$

The temperature variation ϑ_{lf} takes into account

- the influence of the non-linear terms with respect to x. These terms are grouped on the right hand member of the diffusion equation (equation (24)) defining a virtual heat source s_{lf}. This source is estimated through ϑ measurements,
- the influence of the thermal boundary conditions. Even if the boundary conditions, with a deeper physical meaning, could be defined (e.g. linear heat losses under Fourier's conditions), unsteady Dirichlet conditions were considered, and identified from the experimental measurements ϑ^+ and ϑ^- at the specimen extremities.

The goal of the spectral method is to obtain an estimate of $\vartheta_{sp} = \vartheta - \vartheta_{lf}$ from the thermal data ϑ and to use its almost analytical expression to derive the sources $s(x,t)$ from equation (22). The "lifting" temperature variation ϑ_{lf} is estimated through a direct resolution of equation (24) while accounting for the virtual heat source $s_{lf}(x,t)$.

Local Least-Squares Fitting

The local fitting function ϑ_{fit} of the temperature charts is chosen in the same way as in [5]:

$$\vartheta_{fit}(x,t) = P_1(x)t + P_2(x) + P_3(x)\cos(2\pi f_L t) + P_4(x)\sin(2\pi f_L t) \tag{25}$$

where the trigonometric time functions may describe the periodic part of the thermoelastic effects (during cyclic tests), while the linear time function takes transient effects due to heat losses, dissipative heating and possible drifts in the equilibrium temperature into account. In equation (25), f_L stands for the loading frequency. The functions $P_i(x), i = 1,\ldots,4$, are 2^{nd} order polynomials in x. These polynomials enabled us to account for possible spatial heterogeneity in the source patterns. This standard technique applied to the fatigue of steels was fully described in [4]. The main advantages of this method are the robustness with respect to thermal noise and the possibility of separately computing the thermoelastic source amplitude and the mean dissipation per cycle by using under-sampled thermosignals during monochromatic fatigue tests. Naturally for nonmonochromatic cyclic tests, the local approximation function of the temperature $\vartheta_{fit}(x,t)$ can be limited to $\vartheta_{fit}(x,t) = P_1(x)t + P_2(x)$. The local analytical expression of the temperature is then identified in order to compute the different partial derivatives involved in the heat equation. They are then averaged over the approximation zone (Fig. 6) and combined to assess the different calorimetric information.

POD Preprocessing

As with the spectral method, the temperature ϑ is split into two components ϑ_{POD} and ϑ_{lf}, i.e. a new lifting temperature which is slightly different from that used with the spectral method. The 'lifting' temperature ϑ_{lf} is the solution of the thermal problem without heat sources:

$$\begin{cases} \left(\dfrac{\partial \vartheta_{lf}}{\partial t} + \dfrac{\vartheta_{lf}}{\tau_{th}^{1D}(x)}\right) - D\left(\dfrac{S'(x)}{S(x)}\dfrac{\partial \vartheta_{lf}}{\partial x} + \dfrac{\partial^2 \vartheta_{lf}}{\partial x^2}\right) = 0 \\ \vartheta_{lf}(-\frac{L}{2},t) = \vartheta^-(t) \quad \text{and} \quad \vartheta_{lf}(+\frac{L}{2},t) = \vartheta^+(t) \\ \vartheta_{lf}(x,0) = 0 \end{cases} \tag{26}$$

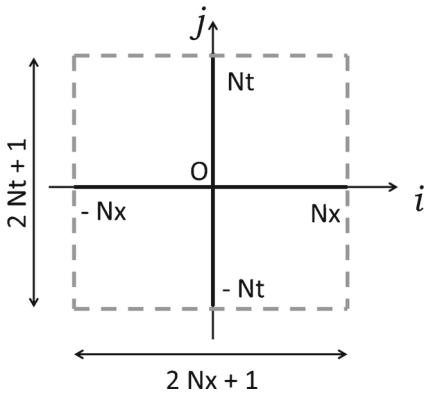

Fig. 6 Size parameters of the approximation zone: $2N_x+1$ and $2N_t+1$ are the numbers of pixels and frames involved in the least-squares fitting, respectively

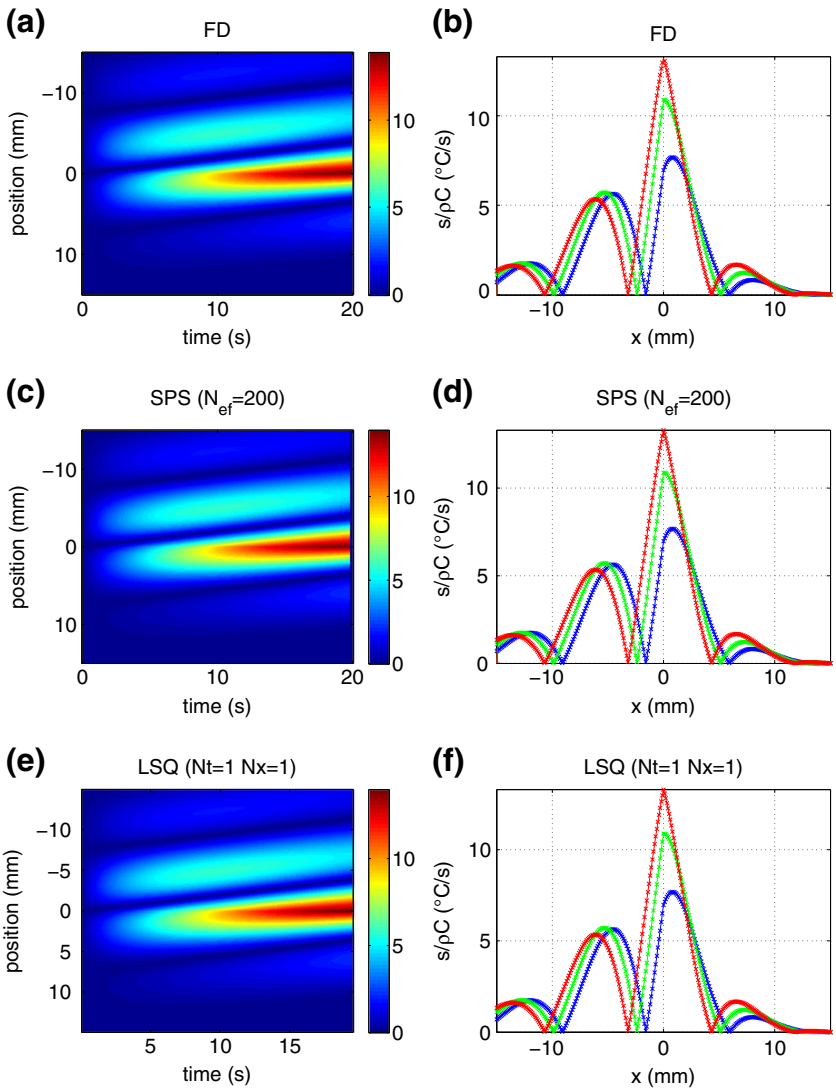

Fig. 7 Heat source assessments derived from θ_{ref} using the three methods: (**a**, **b**) FD, (**c**, **d**) SPS, (**e**, **f**) LSQ. In (**b**, **d**, **f**), s_{ref} are indicated using *dotted lines*

The temperature ϑ_{POD} is then be written as $\vartheta_{POD} = \vartheta - \vartheta_{lf}$ and can be approximated by:

$$\vartheta_{POD}(x,t) = \sum_{k=1}^{N} \left(\int_{-L/2}^{L/2} \left(\vartheta\left(x',t\right) - \vartheta_{lf}\left(x',t\right)\right) \varphi_k\left(x'\right) \mathrm{d}x' \right) \varphi_k(x). \tag{27}$$

Thanks to the linearity of the heat diffusion problem, ϑ_{POD} is the approximated solution of the continuous diffusion problem:

$$\begin{cases} \left(\dfrac{\partial \vartheta_{POD}}{\partial t} + \dfrac{\vartheta_{POD}}{\tau_{th}^{1D}(x)} \right) - D \left(\dfrac{S'(x)}{S(x)} \dfrac{\partial \vartheta_{POD}}{\partial x} + \dfrac{\partial^2 \vartheta_{POD}}{\partial x^2} \right) = \dfrac{s(x,t)}{\rho C} \\ \vartheta_{POD}\left(-\frac{L}{2},t\right) = \vartheta_{lf}\left(+\frac{L}{2},t\right) = 0 \\ \vartheta_{POD}(x,0) = 0 \end{cases} \tag{28}$$

When using this preprocessing procedure, the approximation error $\vartheta - \vartheta_{POD} - \vartheta_{lf}$ is expected to be related to the measurement noise. If this error is more than the measurement noise, the set of putative heat sources has to be extended in order to expand the subspace spanned by the POMs $(\varphi_k)_{k=1,\ldots M}$. To get rid of missing putative heat sources, a point source in space is introduced for each IR element.

In practice, the temperature difference ϑ_{POD} is derived from the thermal data and from the computed lifting temperature. The difference is projected onto the POM basis to considerably reduce the measurement noise. The tempera-

Table 1 Heat source assessments using θ_{ref}

Method	Mean (x 10^{-3} °Cs^{-1})	std (x 10^{-3} °Cs^{-1})	Parameter	CPU time (s)
DF	38	22	–	0.35
SPS	0.3	13	$N_{ef} = 200$	447.6
LSQ	0.3	15	$N_x = 1$ $N_t = 1$	6.3

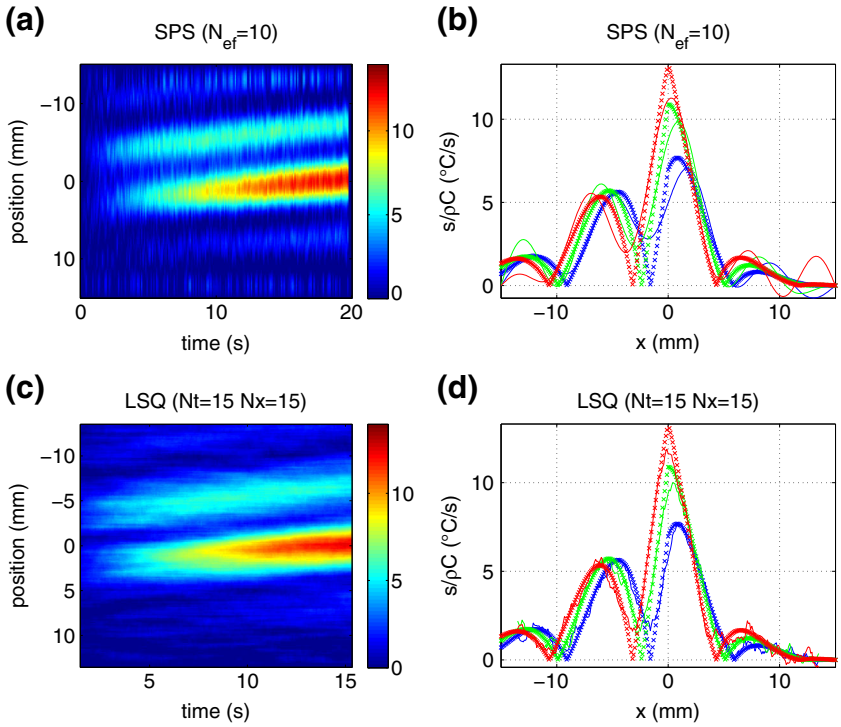

Fig. 8 Heat source assessments derived from noisy data θ_{ref} using the 2 methods: (**a**, **b**) SPS, (**c**, **d**) LSQ

ture field ϑ_{POD} can be used to estimate the different partial differential operators of equation (28) and to assess the heat sources.

Comparative Analysis

This section presents the different heat source assessments obtained with the three different data processing methods. Computations with θ_{ref} (without noise) were first performed to check the consistency (convergence) of the numerical schemes. Then a random noise with a peak-to-peak of about $100mK$ was superimposed to test the robustness of the methods with respect to noise. In a third step, a POD of the thermal data was carried out before the heat source computations. Only the projection of the noisy temperature on the first POMs was retained. This operation eliminates a large part of the noise without degrading the low frequency thermosignal components. Once the noise was reduced, the different data processing results were once again compared with the reference test. Finally, the methods were applied to a thermal dataset extracted from a dynamic fatigue test on pure copper specimens.

Heat Source Assessments Using θ_{ref}

Figure 7 shows the heat source distributions derived from the reference temperature dataset. Following the presentation mode adopted for the benchmark test, a contour plot of sources is systematically shown (left) and three profiles are plotted (right) at three different times ($t_i = 8, 12, 16s$) for each method. To check the efficiency of the methods, reference sources $s_{ref}(t_i, x)$ (dotted lines) were superimposed,

Table 2 Heat source assessments using noisy thermal data

Method	Mean (x 10^{-3} °C/s)	std (x 10^{-3} °C/s)	Parameter	CPU time (s)
FD	–	–	–	–
SPS	−11	726	$N_{ef} = 10$	37.95
LSQ	21	429	$N_x = 15\ N_t = 15$	5.37
POD+FD	1	750	$N_m = 10$	$0.52 + 0.33$
POD+SPS	−12	734	$N_m = 15\ N_{ef} = 10$	$0.61 + 11.64$
POD+LSQ	−9	383	$N_m = 15\ N_x = 10\ N_t = 10$	$0.61 + 5.34$

with full lines representing the computed profiles derived from the thermal data.

Qualitatively, the reconstructed sources closely matched the reference. Their profiles are quasi-undistinguishable.

To quantify the differences between the computed and reference sources, Table 1 shows the mean and standard deviation of these differences. The table naturally specifies the parameter chosen for this comparison. No adjustable parameter was envisaged for the finite difference method. Conversely, the number N_{ef} of eigenfunctions chosen to define the truncated spectral solution, as well as the number of pixels and frames $(2N_x + 1) \times (2N_t + 1)$, involved in defining the local least-squares approximation are indicated. As the thermal data were noiseless, a large number of eigenfunctions could be chosen ($N_{ef} = 200$). In the same way, the approximation zone defined to locally fit the thermal data can also be maximally reduced (3 pixels and 3 frames).

The mean value of s_{ref} over the test is about $2.18\,°\text{C}.s^{-1}$. This can be compared to the mean discard and standard deviations of the differences in order to confirm the consistency of the computational of heat source methods.

CPU times are also indicated. The timing naturally depends on the computer characteristics, programming language, size of thermal dataset to process, etc. Here, only a comparison of these times is really informative. For instance, the spectral method is particularly time consuming. This slowness is due to the fine projection of the thermal data onto the numerous eigenfunctions. For high eigenpulsation, the thermosignal must be interpolated to ensure a quantitatively correct projection, with the scalar product corresponding to a quadrature operation.

Heat Source Assessments Using Noisy Thermal Data

As already underlined, the experimental results always have random noise. To check the robustness of the previous methods, white noise with a uniform distribution, whose peak-to-peak amplitude of 0.1 °C was superimposed on θ_{ref}.

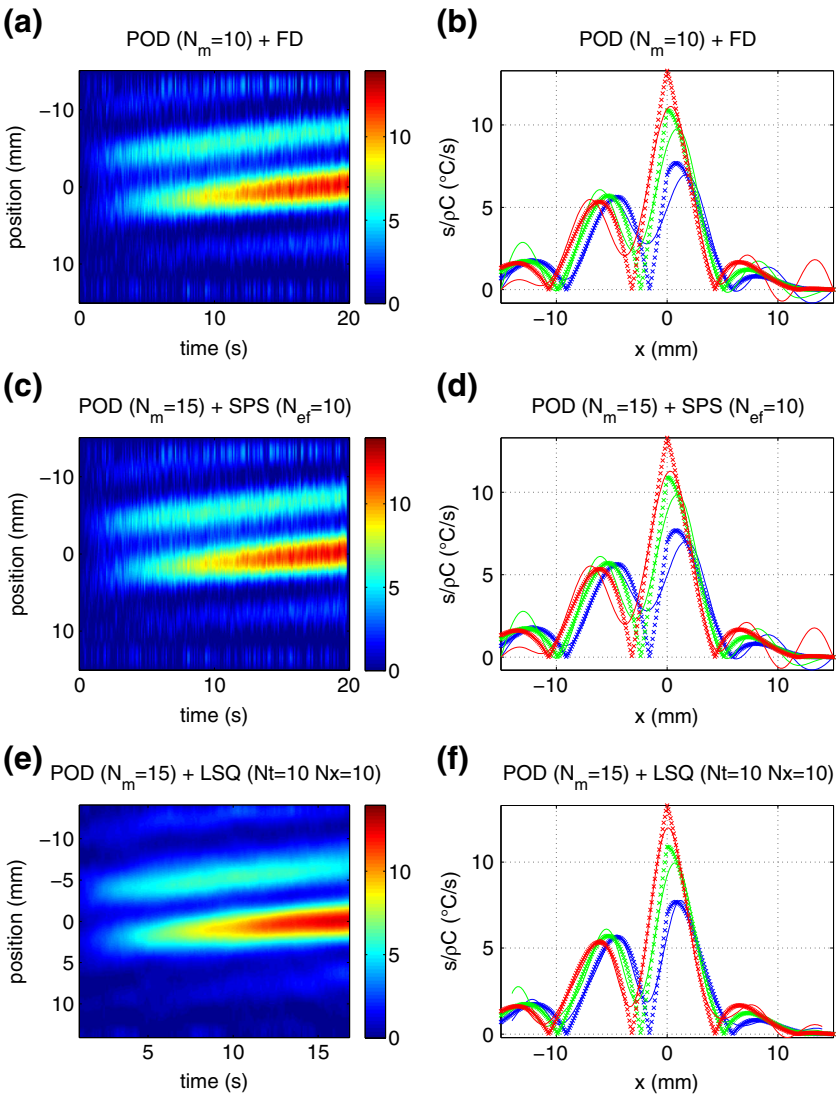

Fig. 9 Heat source assessment with preprocessed thermal data: (**a**, **b**) POD + FD method, (**c**, **d**) POD + SPS method, (**e**, **f**) POD + LSQ method

Direct Assessment

Figure 8 only shows the results obtained with SPS and LSQ methods. The DF method gave too noisy estimates of heat sources that were not plotted. As indicated in the example of Fig. 3(b), the 2nd order derivative of noisy data considerably amplifies the noise.

Both methods gave satisfactory results. The high heat sources were clearly localized. However, more specifically, little wavelets can be seen in Fig. 8(a) and (b). They are due to the time derivation of the spectral solution using simple finite differences. A more efficient way could have been considered here but would have lengthened the already very long processing time. In Fig. 8(c) and (d) the local LSQ fitting of thermal data gave better results. A small residue of noise effects can however be observed on the source profiles (Fig. 8(b)) From a more quantitative standpoint, Table 1 indicates the means and standard deviation of the differences between the reference and computed heat sources. No results were obtained through the FD method. We observed that the mean error value remained low, contrary to the standard deviations, which were 30-fold greater than those obtained with the reference thermal data.

Use of POD before Heat Source Assessment

Before assessing heat sources, it could be interesting to project the thermal data onto the first POMs in order to reduce the noise amplitude. As indicated in Table 2, we used about 10 to 15 modes.

The first result to mention is certainly the fact that the sources could be calculated with the FD method (Fig. 9(a) and (b)). Note that the method gave very noisy results with a convolution filter (Fig. 3(b)). Regarding the SPS method, the quality of the results is similar to that obtained without preprocessing (Fig. 9(c) and (d)). However, the gain in thermosignal regularity allows a more rapid convergence of the projections whose timing is 3-fold lower for the same number of eigenfunctions (Table 2). Finally, regarding the LSQ method, POD slightly improves the standard deviation with respect to the differences between reference and calculated sources (Fig. 9(e) and (f)). The main advantage of POD preprocessing is certainly that it reduces the approximation zone. With the chosen fitting parameters, the size of this approximation zone is 2-fold smaller. As the size of the fitting zone decreases, the fitting function will more precisely describe the local temperature variations and therefore its space and time derivatives, and in turn the local heat sources.

Comparative Analysis of Assessment Methods on Experimental Thermal Data

The chosen experimental data were extracted from a dynamic fatigue test conducted on a pure copper specimen. The specimen shape and its geometrical characteristics are

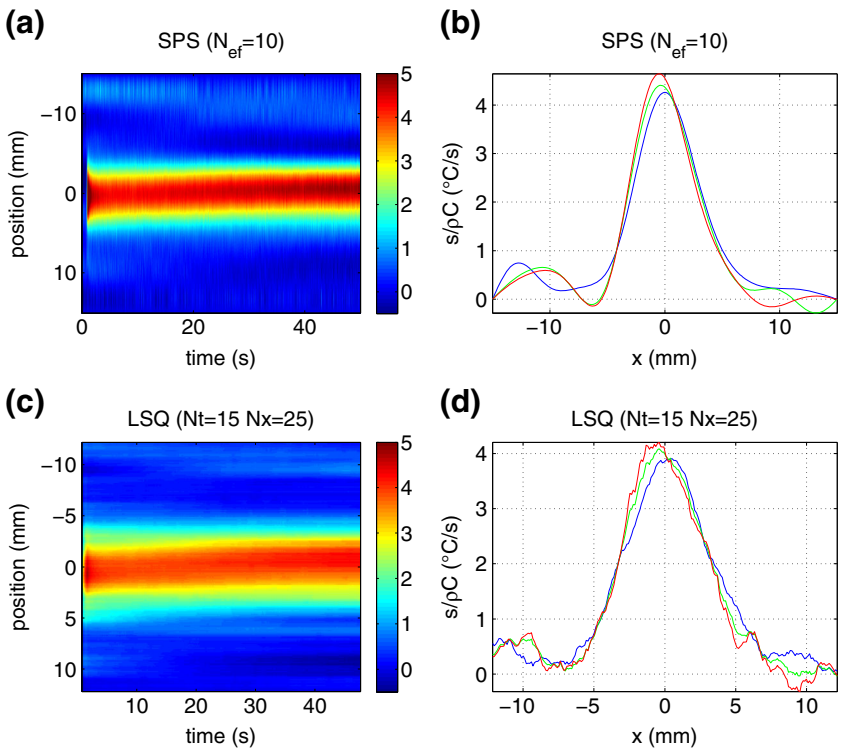

Fig. 10 Heat source assessments: (**a**, **b**) SPS method, (**c**, **d**) LSQ method; the profiles in (**b**, **d**) are captured at times $t = 10, 25, 40s$

indicated in Fig. 1. The loading frequency was about 20 kHz. For this frequency level, the maximum frame rate of the current IRFPA camera is too low to capture the thermoelastic effects. Only the mean dissipative sources per cycle can be estimated [29].

Direct Assessment of Heat Sources

As previously described, the heat sources were first computed without preprocessing of the thermal data using POD. The presentation of results is the same as previously. The results obtained when directly using the FD method were not plotted because of their excessive noise. The other results are shown in Fig. 10(a) and (b) for the SPS method and in Fig. 10(c) and (d) for the LSQ method. Both methods indicate a main heat source concentration in the center of the specimen. A second small bump can be seen on the left part of the specimen. Slight displacement of these maxima was observed throughout the test with the two methods. The main bump moved left while the small bump moved right. Regarding the shape of the high dissipation localization zone, the peak obtained with the SPS method is higher and narrower than that computed with the LSQ method. This crushing of gradients is a classical disadvantage of smoothing techniques. To limit this effect, the fitting zone must be reduced if possible, taking into account of the signal-to-noise ratio.

Heat Source Assessments with Preprocessed Data

In Fig. 11, the last results were obtained after projection of the thermal data onto only the first ten POMs. With such a preprocessed signal, the three methods gave similar results. The shapes of the high dissipation zone are

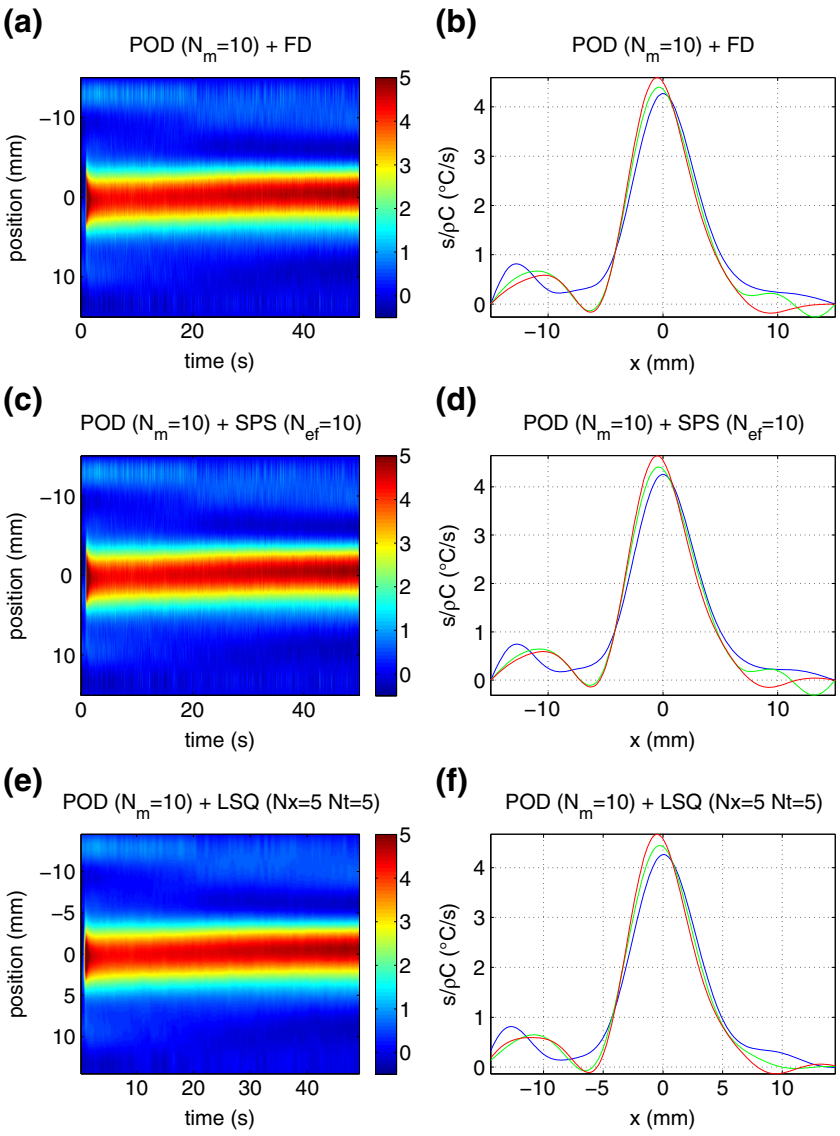

Fig. 11 Heat source assessments with preprocessed data, (**a**, **b**) POD + FD method, (**c**, **d**) POD + SPS method, POD + LSQ method; capture times of profiles $t = 10, 25, 40s$

very close to each other, even those obtained with the LSQ method. Between the processing of Fig. 11(c), (d) (e) and (f), the fitting zone was 13-fold smaller. As already underlined, this decrease in the fitting zone, allowed by the noise reduction, limits the crushing effects. Finally, the displacements of the maximal dissipation zones can also be clearly observed throughout the 10^6 cycles.

Concluding Comments

In this paper, the main goal was to show that the use of a truncated POD of thermal data improves heat source assessments. A 1D benchmark test was thus proposed. Penalizing conditions were systematically chosen to check the robustness of the computational methods. Three methods were tested:

- the first one is based on finite difference estimates of partial derivatives involved in the heat diffusion equation;
- the second uses knowledge of the spectral solution of the diffusion problem;
- the third locally fits the thermal data and the fitting function, determined in the least-squares sense, and is used to estimate heat sources via the heat equation.

The general advantages of POD preprocessing are as follows:

- POMs can be computed once the diffusion problem is defined,
- the number of POMs to be considered in the preprocessing of thermal data can also be determined, once the thermal noise characteristics are known,
- the CPU times necessary to project the thermal data are almost negligible compared with those necessary to compute the heat sources.

Now regarding the specific advantages of POD preprocessing according to each heat source computational method:

- the most remarkable result is certainly that POD allows the operator to 'save' the FD method with noisy thermal data. The noise reduction obtained by truncating the POD solution is better than convolutive filtering or least-squares fitting,
- noise reduction by POD allows us to consider a greater number of eigenfunctions which can be useful when heterogeneous heat source fields develop,
- noise reduction by POD limits the fitting zone and therefore the crushing of thermal gradients.

Considering the data processing, very similar results were obtained with the three methods. In the case of dynamic fatigue testing on pure copper specimens, the heterogeneous source distributions were almost identical. The peak intensity of dissipation and its displacement during the test were achieved by three methods. Here the POD method was used to translate the thermal model, which is assumed to explain the experimental data, into a reduced basis of admissible fields on which the data are projected before any interpretation. Regarding the prospects of this work, improvements in the preprocessing are still likely possible. Indeed, the source computations, using FD and SPS induced ripples that were observed in the time direction. This was certainly due to the fact that the projection of thermal data was on the POMs space (idem for the SPS solution). Would it be possible to reduce these ripples by making a new POD considering the time POMs. Finally, an extension of the preprocessing to 2D diffusion problems is under way. In the 1D example of fatigue, we have seen that the heat source profiles were heterogeneous. This was quite logical here given the shape of the sample. However, heterogeneous fields also appeared for samples whose gage part had a constant cross-section. It is therefore crucial to extend this preprocessing method to 2D thermal fields. Indeed, knowledge of the localization effects is essential to differentiate material effects from structural effects and then to model and identify the constitutive equations of the materials.

References

1. Bathias C, Paris P (2005) Gigacycle fatigue in mechanical practice. Marcel Dekker
2. Batsale C, Chrysochoos A, Pron H, Wattrisse B (2013) Thermomechanical analysis of material behaviors, chap. 16 measurements and identification in solid mechanics. ISBN 978-1-84821-294-7
3. Berkoz G, Holmes P, Lumley JL (1993) The proper orthogonal decomposition in the analysis of turbulent flows. Annu Rev Fluid Mech 25:539–575
4. Berthel B, Chrysochoos A, Wattrisse B, Galtier A (2008) Infrared image processing for the calorimetric analysis of fatigue phenomena. Exp Mech 48(1):79–90
5. Boulanger T, Chrysochoos A, Mabru C, Galtier A (2004) Calorimetric analysis of dissipative and thermoelastic effects associated with the fatigue behavior of steels. Int J Fatigue 26(3):221–229
6. Carlberg K, Cortial J, Amsallem D, Zahr M, Farhat C (2011) The gnat nonlinear model reduction method and its application to fluid dynamics problems. In: 6th AIAA theoretical fluid mechanics conference. Honolulu pp 2011–3112
7. Chaturantabut S, Sorensen DC (2010) Nonlinear model reduction via discrete empirical interpolation. In: Proceedings of the 48h IEEE conference on decision and control CDC held jointly with 2009, 28th Chinese control conference, vol 32. IEEE, pp 2737–2764
8. Chrysochoos A (1995) Analyse du comportement thermomécanique des matériaux par thermographie infrarouge. In: Eyrolles (ed) Photomécanique vol 95, pp 203–211
9. Chrysochoos A (2012) Infrared thermography applied to the analysis of material behavior: a brief overview. Qirt J 9(2):193–208

10. Chrysochoos A, Louche H (2000) An infrared image processing to analyse the calorific effects accompanying strain localisation. Int J Eng Sci 38:1759–1788
11. Chrysochoos A, Wattrisse B, Muracciole JM, El Kaim YE (2009) Fields of stored energy associated with localized necking of steel. J Mech Mater Struct 4(2):245–262
12. Dauvergne JL, Del Barrio E (2010) Toward a simulation-free pod approach for low-dimensional description of phase-change problems. Int J Therm Sci 49(8):1369–1382
13. del Barrio EP, Dauvergne JL (2011) Karhunen-Loève decomposition for data, noise, and model reduction in inverse problems. Taylor & Francis Group, New York, pp 507–539
14. Doudard C, Calloch S, Hild F, Roux S (2010) Identification of heat source fields from infrared thermography: determination of 'self-heating' in a dual-phase steel by using a dog bone sample. Mech Mater 42(1):55–62
15. Everson R, Sirovich L (1995) Karhunen-loeve procedure for gappy data. J Opt Soc Am A 12:1657–1664
16. Fudym O, Batsale J, Battaglia J (2013) Thermophysical properties mapping in semi-infinite longitudinally cracked plates by temperature image processing. Inverse Prob Eng 15(2):163–176
17. Fudym O, Batsale J, Leconte D (2002) A seminumerical approach for heat diffusion in heterogeneous media, one extension of the analytical quadrupole method. Numer Heat Trans Part B 42:325–348
18. Galbally D, Fidkowski K, Willcox K, Ghattas O (2010) Nonlinear model reduction for uncertainty quantification in large-scale inverse problems. Int J Numer Methods Eng 81(12):1581–1608
19. Holmes P, Lumley J, Berkoz G (1996) Turbulence, coherent structures, dynamical systems and symmetry. Cambridge monographs on mechanics. Cambridge University Press
20. Hotteling H (1946) Analysis of complex statistical variables into principal components. Ann Acad Sci Fenn A1(37):3–79
21. Karhunen K (1946) Uber lineare methoden in der wahrscheinlichkeitsrechnung. Ann Acad Sci Fenn A1(37):3–79
22. Loève MM (1955) Probability theory. Princeton
23. Lumley JL (1967) The structure of inhomogeneous turbulence. In: Yaglom T (ed) Atmospheric turbulence and radio wave propagation. Nauka Press, Moscow, pp 166–178
24. Nayroles B, Bouc R, Caumon H, Chezeaux JC, Giacometti E (1981) Infrared telethermography and structures mechanics. Int J Eng Sci 19(7):929–947
25. Park HM, Lee JH (1998) A method of solving inverse convection problems by means of mode reduction. Chem End Sci 53:1731–1744
26. Poncelet M, Witz JF, Pron H, Wattrisse B (2011) A study of irfpa camera measurement errors: radiometric artefacts. Qirt J 8:3–20
27. Ryckelynck D (2005) A priori hypereduction method: an adaptive approach. J Comput Phys 202(N1):346–366
28. Ryckelynck D (2009) Hyper-reduction of mechanical models involving internal variables. Int J Numer Methods Eng 77(1):75–89. doi:10.1002/nme.2406
29. Wang C, Blanche A, Wagner D, Chrysochoos A, Bathias C (2014) Dissipative and microstructural effects associated with fatigue crack initiation on an armco iron. Int J Fatigue 58:152–157
30. Willcox K (2006) Unsteady flow sensing and estimation via the gappy proper orthogonal decomposition. Comput Fluids 35(2):208–226